Earth and Planetary Science Letters 534 (2020) 116044

Contents lists available at ScienceDirect

Earth and Planetary Science Letters

www.elsevier.com/locate/epsl

Carbon isotope and mammal recovery from extreme greenhouse warming at the Paleocene–Eocene boundary in astronomically-calibrated fluvial strata, Bighorn Basin, Wyoming, USA

Bas van der Meulen [a,*,1], Philip D. Gingerich [b], Lucas J. Lourens [a], Niels Meijer [c], Sjors van Broekhuizen [a], Sverre van Ginneken [a], Hemmo A. Abels [d]

[a] Department of Earth Sciences, Utrecht University, Princetonlaan 8a, 3584 CB Utrecht, the Netherlands
[b] Museum of Paleontology, University of Michigan, Ann Arbor, MI 48109-1079, USA
[c] Institute of Geosciences, University of Potsdam, Karl-Liebknecht-Straße 24-25, 14476 Potsdam-Golm, Germany
[d] Department of Geoscience and Engineering, Delft University of Technology, Stevinweg 1, 2628 CN Delft, the Netherlands

ARTICLE INFO

Article history:
Received 18 April 2019
Received in revised form 5 December 2019
Accepted 17 December 2019
Available online 15 January 2020
Editor: L. Robinson

Keywords:
Paleocene–Eocene Thermal Maximum
carbon isotope excursion
initial recovery step
age model
Bighorn Basin
mammalian evolution

ABSTRACT

Massive addition of isotopically-depleted carbon to the ocean and atmosphere caused a carbon isotope excursion (CIE) and global greenhouse warming during the Paleocene–Eocene Thermal Maximum (PETM) circa 56 million years ago. The body of the CIE is followed by a recovery interval that is key to understanding Earth's capacity for carbon uptake, mechanisms of carbon uptake, and biotic responses following an extreme greenhouse warming event. Expanded terrestrial stratigraphic sections in the Bighorn Basin of Wyoming provide exceptionally high-resolution records of the CIE and can be linked directly to the mammalian fossil record.

Here, we provide carbon isotope records of unprecedented resolution measured on in-situ pedogenic carbonate nodules in two parallel 8-km-spaced sections of upper Paleocene and lower Eocene fluvial sediments in the northern Bighorn Basin. We find consistent precession-driven sedimentary cycles in the two sections. Cycle thicknesses show significant lateral, and thus vertical, variation, demonstrating that astronomical age models constructed for fluvial successions require detailed sedimentary facies analysis of parallel sites.

Plotting the high-resolution carbon isotope records in time using our astronomical age model for the correlated sections indicates a CIE body duration of 101 ± 9 kyr. The CIE shows an initial recovery step of +2.7 ± 1.0‰. This step occurs across the single, well-developed paleosol marker bed known as Purple-4, which represents a time interval of up to 15 kyr. The rapidity of recovery at the end of the CIE body is remarkable in light of existing hypotheses for carbon removal from the ocean–atmosphere system. Concurrent mammal finds show that the transition from faunal zone Wa-0 to faunal zone Wa-1 occurred in two steps, with a transitional Wa-R fauna preceding the CIE initial recovery step and Wa-1 fauna following the step.

1. Introduction

The Paleocene–Eocene Thermal Maximum (PETM) is an interval of transient climate change invoked as a model for our near future (Zachos et al., 2008). Massive release of isotopically-light carbon to the ocean–atmosphere system resulted in rapid global warming, ocean acidification, and ecological as well as evolutionary changes (Kennett and Stott, 1991; Koch et al., 1992; Sluijs et al., 2007; McInerney and Wing, 2011). The PETM is recognized in the sedimentary record as a pronounced negative carbon isotope excursion (CIE). Sorting out the shape and timing of the CIE is crucial for unraveling causes and consequences of the PETM (Sluijs et al., 2007; Zeebe et al., 2009).

The duration of the CIE has been established by different methods. Identification of orbitally-forced sedimentary cycles has led to conflicting estimates ranging from circa 157 kyr (Abdul Aziz et al.,

* Corresponding author.
E-mail addresses: b.vandermeulen@uu.nl (B. van der Meulen), gingeric@umich.edu (P.D. Gingerich), l.j.lourens@uu.nl (L.J. Lourens), meijer@uni-potsdam.de (N. Meijer), s.vanbroekhuizen@uu.nl (S. van Broekhuizen), s.vanginneken@students.uu.nl (S. van Ginneken), h.a.abels@tudelft.nl (H.A. Abels).
[1] Present address: Department of Physical Geography, Utrecht University, Princetonlaan 8a, 3584 CB Utrecht, the Netherlands.

https://doi.org/10.1016/j.epsl.2019.116044
0012-821X/

2008), circa 170 kyr (Röhl et al., 2007) and circa 200 kyr (Westerhold et al., 2018), to circa 231 kyr (Giusberti et al., 2007). Time scales based on extraterrestrial Helium-3 concentrations in marine sediments (Murphy et al., 2010) give a duration that is roughly consistent with upper estimates from cyclostratigraphic age models. Existing age models disagree not only on the total duration of the event, but also on the allocation of time to different segments of the CIE.

The recovery of the CIE has been shown to be an order of magnitude more rapid than expected from carbon drawdown by silicate weathering (Bowen and Zachos, 2010), interpreted as accelerated sequestration of organic carbon. However, many carbon isotope records are hampered by a lack of sufficient carbonate material and by relatively low sedimentation rates obscuring detailed temporal resolution. Complete and expanded carbon isotope records, with detailed age control, are therefore needed to firmly establish the rate of carbon isotope recovery.

The mammalian record shows a burst of first appearances early in the PETM (Gingerich, 2003; Gingerich and Smith, 2006; McInerney and Wing, 2011). Artiodactyls, perissodactyls, modern primates, and Hyaenodontidae make their entrance in an event also recognized in Asia and Europe. Substantial mammalian dwarfing is found (Gingerich, 1989) early in the body of the PETM, after which further dwarfing occurred toward the middle of the body (Secord et al., 2012). Recovery in the mammalian record occurs in the transition from faunal zone Wa-0 to zone Wa-1, which is a typical early Eocene Wasatchian fauna lacking dwarfed species (Clyde and Gingerich, 1998). An accurate faunal history along with carbon isotope recovery across the Wa-0 to Wa-1 transition does not yet exist due to complexity of fossil finds (Wood et al., 2008).

The Bighorn Basin provides the best-studied terrestrial deposits of the PETM. The CIE was first found on land at Polecat Bench (PCB; Koch et al., 1992), located in the northern part of the basin (Fig. 1). Later studies provided more detailed isotope records and correlations between the mammalian fossil record and the PETM (Bowen et al., 2001; Gingerich, 2001; Magioncalda et al., 2004; Abdul Aziz et al., 2008). Recently, two overlapping cores were drilled from the top of PCB as part of the Bighorn Basin Coring Project (Clyde et al., 2013). The CIE is recorded in the carbon isotope record measured on pedogenic carbonate from these cores (Bowen et al., 2015) and cyclicity in color reflectance and iron intensity has been used to further constrain the age of the PETM (Westerhold et al., 2018).

Upper Paleocene and lower Eocene sediments of the Bighorn Basin exhibit alternations that have been related to autocyclic behavior of the fluvial depositional system (Clyde and Christensen, 2003) and to allocyclic forcing (Kraus and Aslan, 1993; Abdul Aziz et al., 2008). Abels et al. (2013) provided a model in which overbank deposition phases alternate with regional-scale avulsion phases, driven by precession-related climate changes. Precession forcing of the circa 7-m-thick avulsion–overbank cycles is corroborated by circa 34-m-thick eccentricity-related cycles, recently documented in the northern Bighorn Basin (Abels et al., 2016). However, it was observed that the fluvial sequences show high lateral variability and that a single record documents variability related to external forcing as well as internal fluvial processes. The cyclostratigraphic age models for the PETM in the Bighorn Basin of Abdul Aziz et al. (2008) and Westerhold et al. (2018) are based on a single section, and should be verified by the use of multiple records crossing the PETM to disentangle regional, precession-driven cyclicity from internal variability.

Here, we present detailed alluvial stratigraphies of the PCB outcrops and of a new PETM section called Head of Big Sand Coulee (HBSC), located 8 km to the west of PCB (Fig. 1). New high-resolution $\delta^{13}C$ records measured on pedogenic carbonate nodules show the onset, body, and recovery phases of the CIE in unprecedented detail. The sections are correlated based on paleosol marker beds and the CIE onset, and orbitally-forced sedimentary cycles are identified following the methodology of Abels et al. (2013). We use the sedimentary cyclicity to construct a floating astronomical age model for the $\delta^{13}C$ records, providing age constraints for the body and the recovery of the PETM. Detailed analysis of the onset interval will be the focus of a following study. As a last step, we integrate the new high-resolution composite isotope record with an overview of mammalian fossil finds, including new discoveries, in the body of the CIE interval at PCB, in order to fine-tune relations between CIE recovery and mammal faunal recovery.

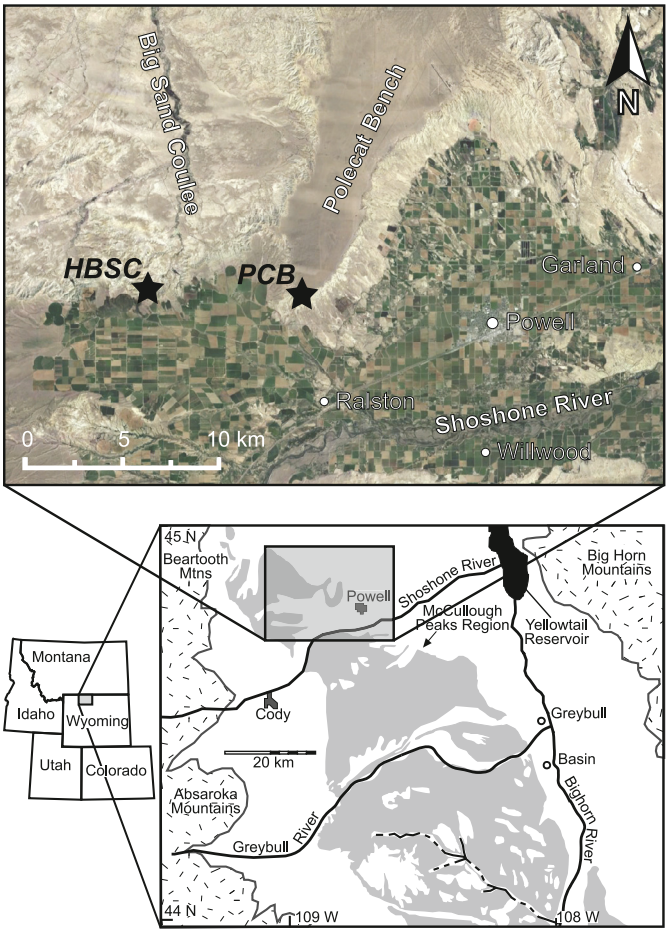

Fig. 1. Locations of the Head of Big Sand Coulee (HBSC) and Polecat Bench (PCB) sections in northern Wyoming. The background satellite image in the upper map is from Google Earth. The lower map is modified from Clyde and Christensen (2003). The gray areas on this map represent exposures of the Eocene Willwood Formation and the stippled areas are surrounding mountain ranges.

2. Methods

2.1. Field research and sample collection

In the HBSC and PCB sections we recorded the lithostratigraphy, measured sediment matrix colors, and collected carbonate nodules. Tracing laterally continuous paleosols between subsections enabled the construction of stratigraphically continuous sections. Trenches of 0.5 to 1 m wide and 0.5 to 1 m deep were dug to study the fresh rock and record sedimentary successions at centimeter scale. Sedimentary facies were distinguished based on grain size, color, and pedogenic features such as slickensides, carbonate nodules, organic content, and color mottling. Of these features, both abundance and size were qualitatively recorded, and carbonate nodules, when present, were sampled at 12.5 cm resolution. Matrix and

mottling colors were determined using Munsell soil color charts. In addition, continuous color reflectance records of the sediment matrix were obtained in the field at 12.5 cm resolution for PCB and most of HBSC, and at 25 to 50 cm resolutions for thick sandstone intervals in HBSC. This was done using a handheld photospectrometer (Konica Minolta CM-600d), yielding reflectance data at 10 nm wavelength intervals between 360 and 740 nm, and derivative lightness (L*), redness (a*), and yellowness (b*) records. Color reflectance was measured in the shade on freshly broken pieces of excavated rock. Unit thicknesses and sampling intervals were measured with a Jacob's staff equipped with a precision Abney level. The base and top of the recorded interval at PCB correspond to meter levels 1440 and 1580 above the K–Pg boundary (Gingerich, 2001).

2.2. Soil Development Index and spectral analysis

Degrees of pedogenesis were assessed using the Soil Development Index (SDI) of Abels et al. (2013), who developed the SDI on a record of early Eocene fluvial sediments in the Bighorn Basin. The sections in this study consist of similar sediments, making the SDI a suitable proxy for pedogenesis at HBSC and PCB. With the SDI, each paleosol profile is assigned a value based on its B-horizon thickness, maximal rubification, and degree of soil horizon development, with respect to the other profiles in the section. Weakly developed paleosols have SDI values <0.5, intermediate pedogenesis yields SDI values between 0.5 and 1.0, and an SDI >1.0 indicates intense pedogenesis (Abels et al., 2013).

Time series analyses on SDI and color records were performed using the Blackman–Tukey method in Analyseries 1.1 (Paillard et al., 1996). The analyses were carried out using compromise settings and a Bartlett window type. Wavelet analyses were performed on the L* records of both sections using the wavelet transform with Morlet mother wavelet (Torrence and Compo, 1998) as implemented in the Acycle software (Li et al., 2019). Subsequently, Gaussian bandpass filters were applied to the records using the dominant periodicities obtained from the previous analyses.

2.3. Stable isotope measurements

Carbonate nodules were carefully broken and subsequently studied at 40x magnification using a binocular microscope in order to identify and sample the microcrystalline carbonate mud (micrite) that usually constituted most of the nodule. Coarse crystalline calcite (sparite) often yields atypical stable isotope values (Bowen et al., 2001; Foreman, 2014) and was therefore avoided. The selected micrite material was ground using a mortar and pestle, and for each sample approximately 100 µg was weighed into a vial. The vials were flushed with helium, orthophosphoric acid was added, and stable isotope ratios were measured in a Thermo Finnigan GasBench II coupled to a Delta V Isotope Ratio Mass Spectrometer at Utrecht University. Sixteen reference carbonate samples were included in each mass spectrometry run of 78 samples. Naxos core marble was used to correct for trends in sample measurements, and IAEA-CO-1 to express the results on the Vienna Pee Dee Belemnite (VPDB) scale. Analytical reproducibility (1σ) based on standards and replicate measurements was better than 0.10‰ for δ^{13}C and better than 0.25‰ for δ^{18}O. Samples with low δ^{18}O values are likely to contain admixtures of sparite (Koch et al., 1995; Bowen et al., 2001) and were excluded from the results. A cut-off point of -10‰ was chosen after Bowen et al. (2001, their Table 1), resulting in the removal of 92 of the 1568 measurements (6% of the original dataset).

2.4. Age model construction

Marker beds labeled by Gingerich (2001) that could be recognized with confidence in both HBSC and PCB were used to correlate the two sections. Following the approach of Abels et al. (2013), we placed sedimentary cycle boundaries at facies transitions where SDI values decrease significantly and abruptly. These cycles were related to precession, based on independent dating evidence from magnetostratigraphy, biostratigraphy and event stratigraphy (Abdul Aziz et al., 2008; Abels et al., 2013, 2016; Westerhold et al., 2018). We adopted a constant duration for the cycles of 20.66 kyr (average precession duration in Paleocene–Eocene times, see Supplementary Information). We then constructed a floating astronomical age model by linear interpolation between avulsion–overbank cycle tops, and used this model to plot the δ^{13}C records in time relative to the onset of the CIE. The 0-kyr level in the age model is placed in between the last pre-onset (circa -10‰) and the first onset (circa -14‰) δ^{13}C values.

3. Results

3.1. Sedimentary facies

The HBSC and PCB sediments range from coarse-grained, drab-colored sandstones with no pedogenic features to fine-grained, red and purple mudstones containing carbonate nodules and other indicators of pedogenesis. These lithologies are distinguishable from a distance because of their contrasting colors when exposed (Fig. 2).

In the Paleogene fluvial sediments of the Bighorn Basin, two main facies are distinguished besides trunk channel sandstones, namely heterolithic avulsion-belt deposits and fine-grained overbank deposits (Kraus and Aslan, 1993; Abels et al., 2013). The heterolithic facies consist of sandstones and incipient paleosols. The fine-grained facies consist of cumulative paleosols with a variety of colors; the dominant color is usually red, but can range from gray to purple. Avulsion and overbank intervals alternate in a relatively regular fashion (Fig. 2), with dominant avulsion–overbank cycles related to precession (Abels et al., 2013, 2016).

3.2. Soil Development Index and color

The SDI records objectively distinguish between the heterolithic and muddy facies (Fig. 3). Sands and silts with occasional weakly-developed paleosols have SDI values below 1.0, whereas SDI values of clear paleosol profiles exceed 1.0. The PETM interval shows an overall increase in paleosol thickness, rubification, and soil horizon development, and therefore also in SDI. Soil characteristics that are not included in the SDI calculation (e.g., nodule and slickenside sizes and abundances, thicknesses of soil eluviation horizons) also increase in the PETM interval. Supplementary Table S1 provides the SDI input data and output values for the respectively 112 and 110 paleosol profiles in the HBSC and PCB sections.

Lithology and color are related, but most relations are not consistent throughout the sections (Fig. 3). Paleosols yield low L* and high a* values, except for gray soil horizons which yield low L* and low a* values. Sandstones yield high L* and low a* values, with higher a* in coarse sandstones. The b* values follow the L* record for intervals with gray soils. Supplementary Table S2 gives the derivative color reflectance values for HBSC (1456 measurements) and PCB (1136 measurements).

3.3. Avulsion–overbank cycles

We distinguish 24 avulsion–overbank cycles in the HBSC and PCB sections (Fig. 3). Many distinct paleosols labeled as marker

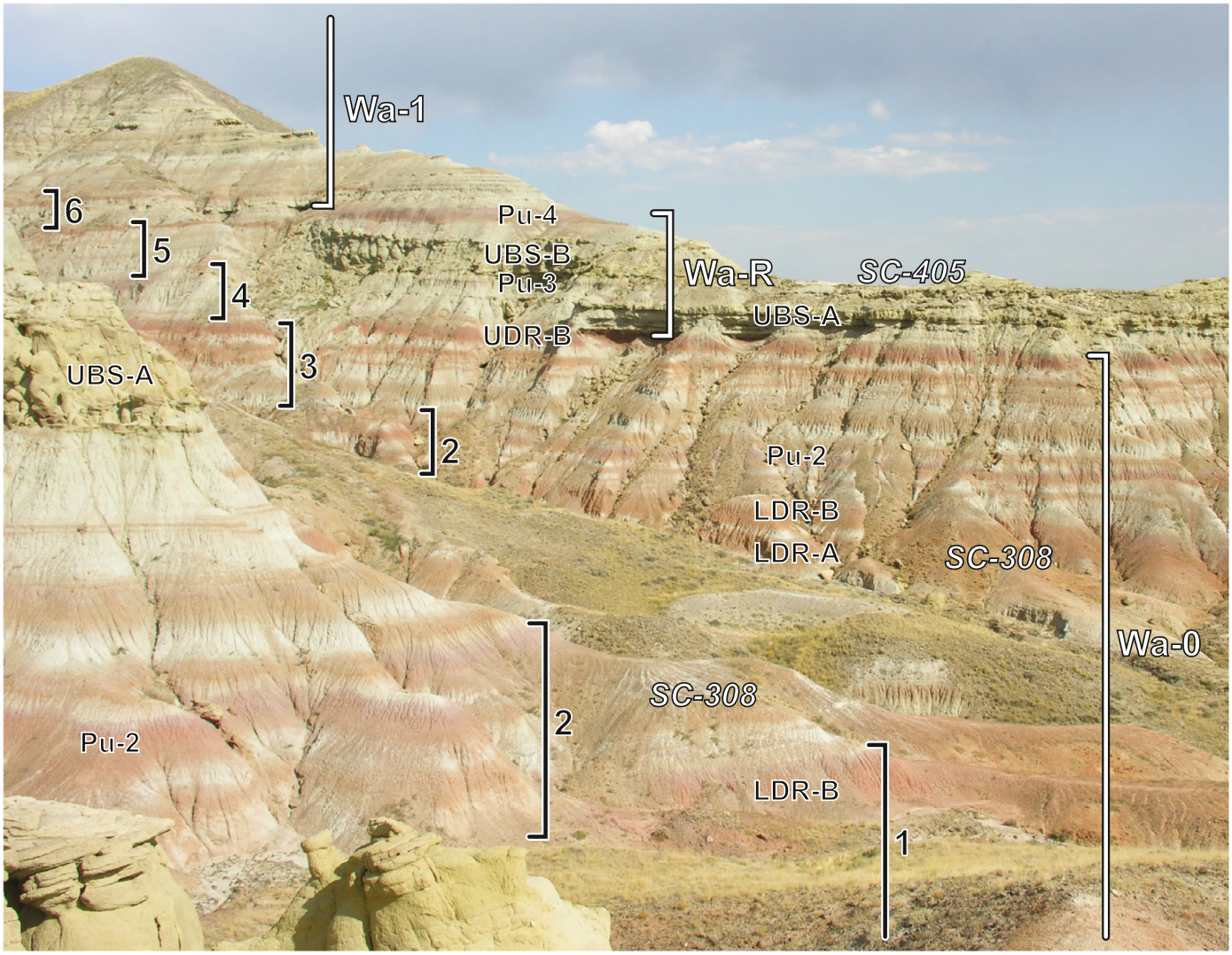

Fig. 2. PETM body to recovery interval in the Polecat Bench section. Marker beds (Gingerich, 2001; Fig. 3) are indicated with abbreviations, as are fossil localities (Fig. S3) and faunal zones (Fig. 7). Avulsion–overbank cycles are indicated and numbered with respect to the first cycle in the PETM (Fig. 3). View is to the northeast and vertical field of view is circa 60 m. LDR = Lower Double-Red, Pu = Purple, SC = Sand Coulee, UBS = Upper Boundary Sandstone, UDR = Upper Double-Red, Wa = Wasatchian. (For interpretation of the colors in the figure(s), the reader is referred to the web version of this article.)

beds (Gingerich, 2001) coincide with avulsion–overbank cycle tops. Robust correlation between cycles in HBSC and PCB indicates lateral consistency of the cycles over a distance of at least 8 km. One exception is the absence of the Lower Double-Red paleosols in HBSC, where instead a coarse-grained unit is present that contains pebbles and decimeter-scale cross-bedding. This unit is laterally correlated to the Boundary Sandstone, which is linked to the CIE and formed as a result of PETM-related climate extremes (Foreman, 2014). Erosion and deposition within a channel obscured cycle 1 at HBSC. The top of this cycle is tentatively placed at the top of the fine-grained interval at 94 m in HBSC (Fig. 3). This does not induce uncertainty in subsequent analyses, because the cycle is well developed at PCB.

Stratigraphic levels and thicknesses of avulsion–overbank cycles are given in Supplementary Table S3. The average cycle thickness is 8.0 ± 1.4 m in HBSC and 7.6 ± 1.3 m in PCB. Between HBSC and PCB, individual cycles show thickness differences up to 3.9 m, demonstrating substantial lateral variation in sedimentation during correlative time intervals. Both sections exhibit a slightly decreasing general trend in cycle thickness (Fig. 4).

Power spectra of SDI and L* show peaks around a period of 7.5 m (Fig. 5; Fig. S1). In the PCB section, also a* shows this peak (Fig. 5). Additionally, a clear peak around a period of 35 m is present in the L* record of PCB (Fig. S1). Gaussian bandpass filters with a bandwidth of 5.0 to 12.5 m are given for all records (Fig. 3). The wide bandwidth is necessary to cover the observed lateral, and thus vertical, variability of sedimentary cycle thicknesses. The SDI and L* filters show opposite trends. In general, the a* filters follow the SDI filters and the b* filters follow the L* filters. However, the a* filter has little power in the lower and upper parts of the sections, and the b* filter has little power in the central to upper parts of the sections.

3.4. Stable isotope data

The pedogenic carbonate $\delta^{13}C$ records of HBSC and PCB show similar trends (Fig. 3) with baseline values around −8‰ that decrease to around −10‰ below the onset of the CIE. The main onset occurs as a relatively sharp decrease in both sections. Throughout the body of the CIE, $\delta^{13}C$ values gradually increase. This increasing trend appears stepwise in the HBSC record, with steps approximately paced by avulsion–overbank cycles. However, the spread in stable isotope values prevents robust recording of these

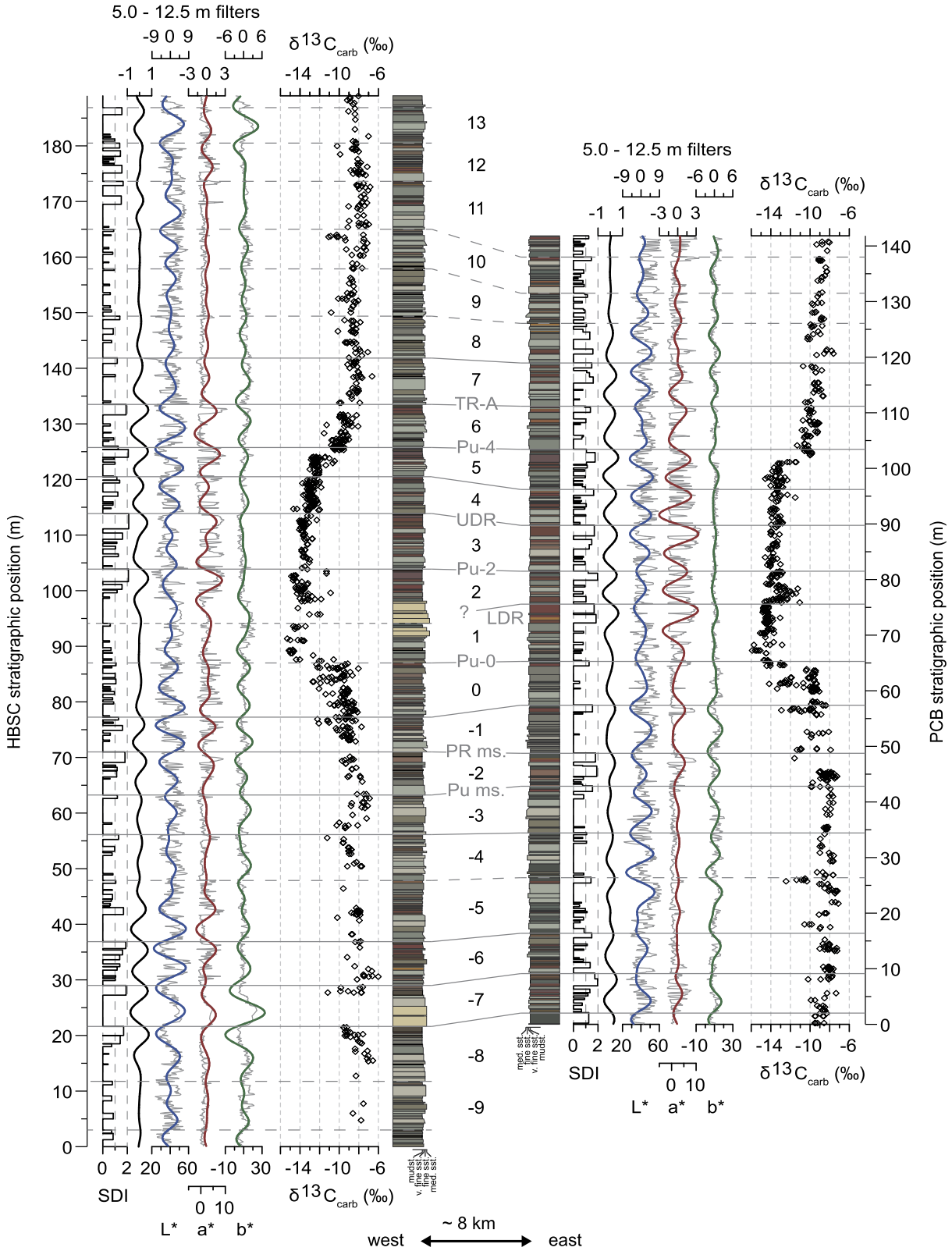

Fig. 3. Head of Big Sand Coulee (HBSC) and Polecat Bench (PCB) sections with lithology, records and Gaussian bandpass filters of Soil Development Index (SDI), lightness (L*), redness (a*), and yellowness (b*), and pedogenic carbonate $\delta^{13}C$ data expressed in per mille on the VPDB scale. Horizontal lines indicate sedimentary cycle transitions from overbank to avulsion facies. Numbering of the cycles is relative to the first cycle in the CIE. Marker beds identified by Gingerich (2001) are indicated with abbreviations. LDR = Lower Double-Red, ms. = mudstone, PR = Purple-Red, Pu = Purple, TR = Top Red, UDR = Upper Double-Red.

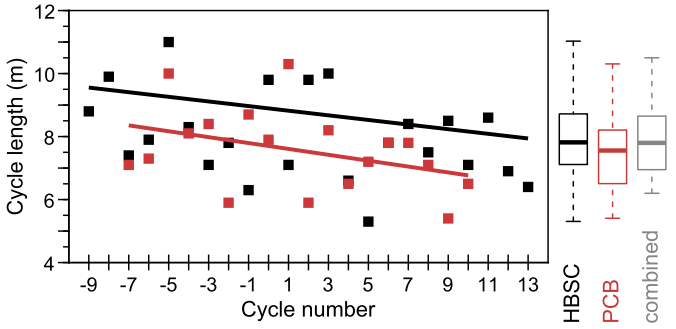

Fig. 4. Thicknesses of corresponding avulsion–overbank cycles in HBSC (black symbols) and PCB (red symbols). Regression lines for both series show a trend toward shorter cycles. See Fig. 3 for the numbering of the cycles; number 1 is the first cycle within the PETM.

possible δ^{13}C-cycles and they do not appear clearly in the PCB record.

A remarkable interval of relatively enriched δ^{13}C values occurs after the first avulsion–overbank cycle above the Lower Double-Red paleosols in PCB (Fig. 3). This minor positive excursion of +1.7 ± 0.7‰ is accompanied by a small negative change in oxygen isotope values of −0.7 ± 0.6‰. At HBSC, this stratigraphic interval is represented by sandstones lacking pedogenic nodules, but some heavier δ^{13}C values are recorded (Fig. 3).

The transition from CIE body to recovery is characterized by a distinct stepwise shift. This initial recovery step (IRS) in δ^{13}C values is +2.3 ± 0.7‰ at HBSC and +3.0 ± 0.7 ‰ at PCB, which combines to +2.7 ± 1.0‰. In both records, the IRS occurs across the Purple-4 marker bed. The last pre-recovery values occur just below the base of the purple B-horizon; the first post-body values are registered in the very top of this same horizon (Fig. 3).

Supplementary Table S4 provides the stable isotope data for HBSC (799 measurements of both δ^{13}C and δ^{18}O) and PCB (677 measurements of both δ^{13}C and δ^{18}O). The δ^{18}O records do not exhibit clear trends, except for slight (circa 0.5‰) enrichment throughout the PETM.

3.5. Durations of CIE intervals

When plotted against time, the IRS and other features in the HBSC and PCB δ^{13}C records line up well (Supplementary Information), confirming the use of avulsion–overbank cycles as time intervals. Combining the records into one composite shows that the CIE body spans 101 ± 9 kyr (Fig. 6). The calculation of the uncertainty is discussed in paragraph 4.2.

The amount of time represented by the IRS in marker bed Purple-4 is unknown, but we find no indication that the marker bed represents more than the regular duration of an overbank phase within one precession cycle. Purple-4 is distinctive and thick, but so are other paleosols, such as Lower Double-Red, Purple-2, and Upper Double-Red. However, Purple-4 lacks pedogenic carbonate nodules, which is a key difference from all other paleosols in the PETM body interval. Purple-4 can be traced for several hundreds of meters in the field in the HBSC and PCB outcrop areas, and shows no signs of fluvial incision. Incision related to the Upper Boundary Sandstone (UBS; Wood et al., 2008) does not coincide with Purple-4 soil formation, as the UBS is overlain by red mudstones followed by Purple-4 (Fig. 2). Thus, this incision predates the IRS.

The duration of the recovery interval depends on the placement of the end of the recovery, which is difficult due to the gradual return of carbon isotope values. The end of the recovery may be placed where the trend of increasing δ^{13}C values stabilizes, circa 40 kyr after the IRS (Fig. 6). However, some 80 kyr later

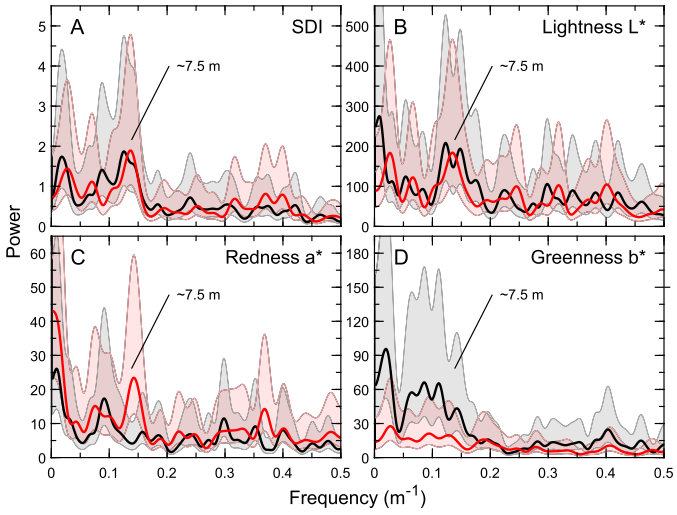

Fig. 5. Blackman–Tukey power spectra with 90% confidence intervals for A) Soil Development Index, B) lightness, C) redness, and D) yellowness, for the Head of Big Sand Coulee (black lines) and Polecat Bench (red lines) sections. Peaks around a period of 7.5 m, which are related to precession, are labeled. Note that frequencies above 0.2 cycles m^{-1} (periods below 5 m) are most likely the result of autocyclic variation.

even higher values are reached. These values are closer to but still somewhat lower than baseline values preceding the CIE. This point, circa 120 kyr after the IRS and 220 kyr after the onset of the PETM, matches with the majority of previous studies concerning the timing of the CIE.

3.6. Mammalian recovery

The transition from a PETM mammalian fauna (zones Wa-M and Wa-0) to a post-PETM fauna (zone Wa-1) is best documented at PCB (Gingerich, 1989), but even here the recovery is difficult to study because of the steepness of outcrops and some downslope fossil contamination (Wood et al., 2008). A state-of-the-art overview of mammalian faunal finds at the southwestern end of Polecat Bench (Supplementary Information) shows that Wa-0 faunas occur lower than Purple-4 and the Upper Boundary Sandstone, and Wa-1 faunas occur above Purple-4.

The stratigraphic interval between marker beds Purple-3 with a Wa-0 fauna and Purple-4 with a Wa-1 fauna contains an intermediate fauna with both Wa-0 and Wa-1 elements (Supplementary Information). We call this fauna Wa-R (Fig. 7). Wa-R has been found in locality SC-405, which is in the UBS. The most interesting mammalian specimen from this locality is a specimen of *Ectocion* with a first lower molar intermediate in size between those of *Ectocion parvus* and those of *Ectocion osbornianus*. Faunal assemblages in the UBS described by Wood et al. (2008) are Wa-R faunas, as are new finds in between the UBS and Purple-4 (Supplementary Information).

4. Discussion

4.1. Avulsion–overbank cycles

The remarkably cyclic nature of the Paleogene strata in the Bighorn Basin has long been observed (Gingerich, 1969; Neasham and Vondra, 1972; Kraus and Aslan, 1993; Clyde and Christensen, 2003). The dominant sedimentary cycles are forced by precession-driven climate change (Abels et al., 2013, 2016) and can therefore be used to assess accumulation rates. Kraus et al. (2015) interpreted the high degrees of pedogenesis in the PETM interval as

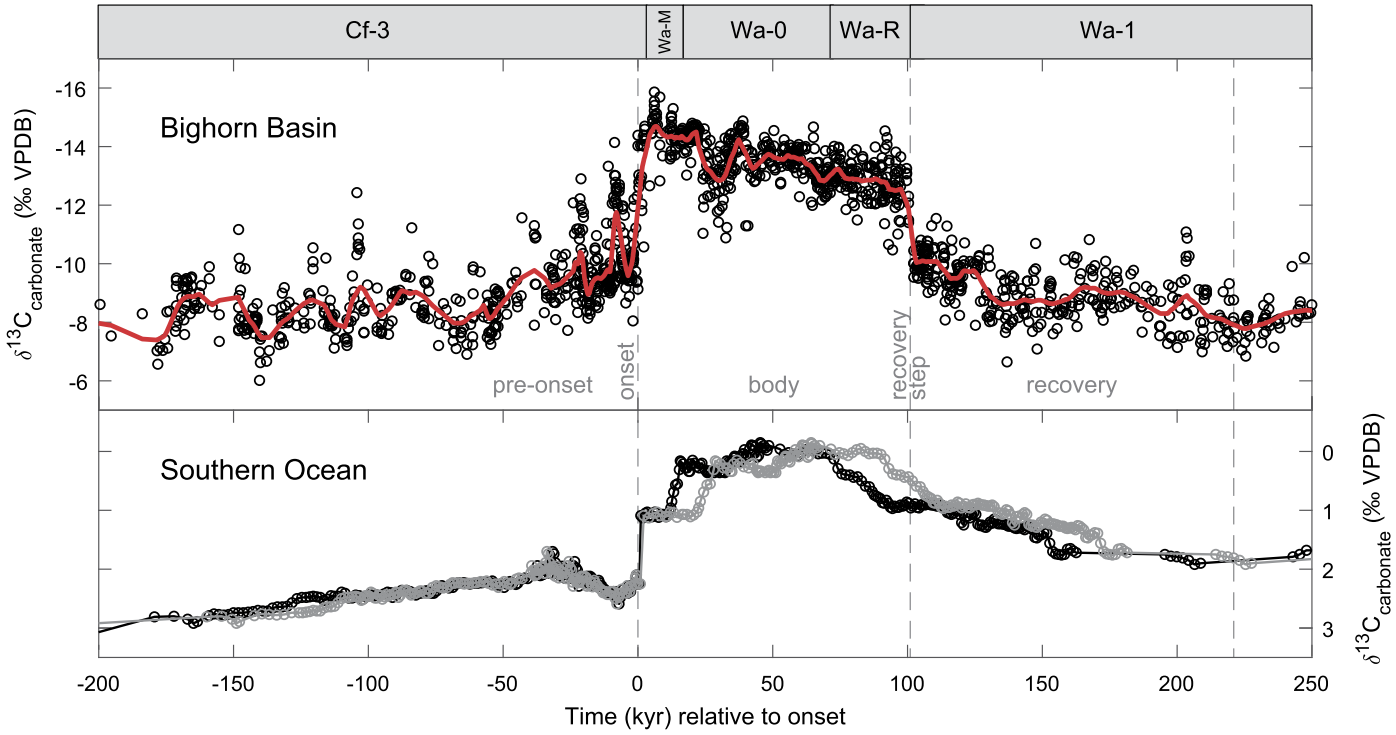

Fig. 6. Northern Bighorn Basin composite $\delta^{13}C$ record plotted in time relative to the onset of the PETM, based on the precession-related avulsion–overbank chronology. The red line is a smoothed version of the record computed by locally weighted linear regression (LOWESS) using a 2.5% window. Indicated above are abbreviated North American land-mammal zones, including the new Wa-R zone. The lower panel shows the bulk carbonate $\delta^{13}C$ record from ODP site 690 (Bains et al., 1999) plotted using the cyclostratigraphic age models of Röhl et al. (2007; black symbols and line) and Westerhold et al. (2018; gray symbols and line).

an indication of lower accumulation rates compared to the underlying and overlying intervals. However, there are no significant changes in avulsion–overbank cycle thicknesses across the PETM (Fig. 4). This strongly implies that, during the PETM, no changes in sediment supply and deposition occurred above the precession time-scale in the northern Bighorn Basin. Instead, the abundant and well-developed paleosols resulted from the exceptional climate in a more direct way than through changes in sedimentation rate; for example, precipitation-related soil drainage can influence soil development and paleosol appearance (Kraus et al., 2013).

On a timescale longer than the PETM, cycle thicknesses decrease by circa 1 m in both sections (Fig. 4). On even longer timescales, cycle thicknesses are relatively stable. Cycles are circa 8 m thick in the interval studied here, in biozone Wa-0 and the PETM, while cycles are circa 7 m thick in biozone Wa-5 and the Eocene Thermal Maximum 2, postdating the PETM by some 2 million years (Abels et al., 2012, 2016; Westerhold et al., 2018). The observed trend in cycle thickness may suggest a decrease in accommodation space creation from the Paleocene into the Eocene, but may also be influenced by the fact that we have only two parallel sites. Unfortunately, more records are not easily available, because outcrops are poor east of Polecat Bench, and thick lower and upper PETM boundary sandstones prevent assessment of avulsion–overbank cycles in the PETM interval west of Head of Big Sand Coulee.

Large thickness differences in fluvial sedimentary cycles between different sites in the Bighorn Basin may have been anticipated, but were not documented prior to this study. The avulsion–overbank cycles are now shown to be laterally consistent over distances of at least 8 km. The large lateral variability in cycle thicknesses (Fig. 3; Fig. 4), indicates meter-scale paleotopographic differences created by fluvial processes. These differences are compensated during subsequent precession cycles (Fig. 3); therefore, sedimentation rates at supra-precession time scales are approximately constant. The average cycle thickness in the HBSC outcrops is 0.4 m larger than in the PCB outcrops (Table S3). This dissimilarity may be attributed to the different basinal locations of the sections. HBSC is located closer to the basin axis (Gingerich and Clyde, 2001), which may have resulted in the creation of more accommodation space and thus larger accumulation rates than at PCB.

The background variability in $\delta^{13}C$ values is large (Fig. 3; Fig. 6); therefore, very high-resolution records are required to solve crucial details such as the IRS. High-resolution records are also required in alluvial sedimentary successions because these are by nature discontinuous, characterized by pulses of sedimentation and episodes of non-deposition and erosion. In the case of the Bighorn Basin, such discontinuities are considered to be no problem on time scales longer than circa 10 kyr and an external climate signal may be preserved, while on shorter time scales a stochastic fluvial signal dominates (Foreman and Straub, 2017). We argue that by using multiple, parallel series, the sampling resolution of climate change through time can still be improved to below 10 kyr. This is because at different places on the floodplain, different snapshots of time are preserved. Measuring records at the highest resolution possible and then compiling composite records may yield crucial patterns, such as the initial recovery step found here.

4.2. Precession-based age model

The large variability in avulsion–overbank cycle thicknesses results in wide spectral peaks for the different lithological proxies (Fig. 5). Cycles of 5 to 11 m may represent the same amount of time. Because of this large range, bandpass-filtered proxy records do not precisely align with observed facies transitions (Fig. 3; see also Abels et al., 2013). This introduces problems when constructing astronomical age models by counting peaks in bandpass-filtered records without interpretation of sedimentary facies. The

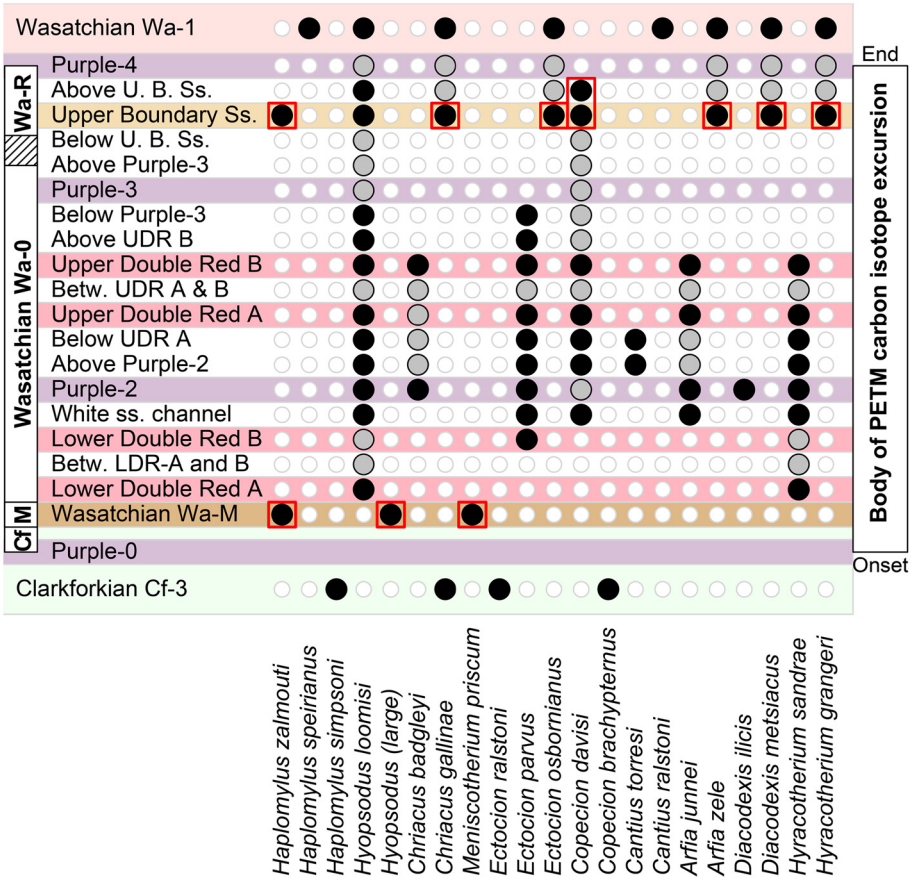

Fig. 7. Detailed range chart for the PETM interval in the northern Bighorn Basin. The Wa-R zone, found in and above the Upper Boundary Sandstone, but below Purple-4, is new. Black circles are actual positively-identified taxon records; gray circles are interpolated between black circles to give a sense of taxon range. Red boxes highlight taxon occurrences distinctive of Wa-M and Wa-R before and after Wa-0. The faunal zones given here are also depicted above the northern Bighorn Basin composite $\delta^{13}C$ record and PETM age model in Fig. 6.

PETM interval at PCB illustrates this, as the bandpass filter of a* shows 5.5 cycles between the onset and the initial recovery step (Fig. 3; see also Abdul Aziz et al., 2008; Westerhold et al., 2018), whereas our integrated analysis of two parallel sections clearly shows at most 5 avulsion–overbank cycles in the CIE body. We conclude that cycle counting in individual sections or cores in such variable depositional settings is unlikely to produce astronomical age models that are reliable at a detailed (i.e., precession) scale. Parallel records are also required to avoid miscounting of cycles due to erosion, illustrated in the PETM interval at HBSC by the thick sand body that locally obscures cycle number 1 (Fig. 3).

Furthermore, the relation between a* and lithology is not consistent. Below the PETM, where abundant gray paleosols and relatively coarse sands occur, the relation between a* and lithology is opposite compared to the PETM interval with abundant red paleosols (Fig. 3). Therefore, the allocation of cycles in long sediment records in the Bighorn Basin can be improved by using L* instead of a*, which has previously been used (Abdul Aziz et al., 2008; Abels et al., 2012; Westerhold et al., 2018). However, for detailed astronomical age models, identifying cycle boundaries using sedimentary facies is still required, as done in this study.

Our age model adopts a precession forcing of avulsion–overbank cycles and assumes a constant phase relation of sedimentary facies with precession-scale climate change. Within the precession cycles, the chronology assumes linear time distribution. However, avulsion and overbank sedimentation rates differ. Therefore, the age model is not accurate at sub-precession time scales. Still, the assumption of linear time distribution within cycles is appropriate when determining the duration of the CIE body interval, since both the onset and the end of the CIE body occur in similar lithologies at similar positions within an avulsion–overbank cycle (Fig. 3).

A remaining uncertainty for determining the exact duration of the PETM body lies in the duration of the precession cycle. This has been ignored in previous cyclostratigraphic age models. Individual precession cycles do not last precisely 21 kyr (present day) or 20.66 kyr (Paleocene–Eocene). Instead, this duration is the average of a multitude of frequencies in the precession band. To quantify the uncertainty related to this assumption, we calculated a standard deviation for the duration of an interval consisting of 5 consecutive precession cycles (Supplementary Information), which yields 9.3 kyr, or about 1.9 kyr per precession cycle.

4.3. Comparison to the marine record

There is significantly more spread in the Bighorn Basin pedogenic carbonate $\delta^{13}C$ record than in marine carbonate $\delta^{13}C$ records (Fig. 6). High-frequency variations in atmospheric isotopic composition are obscured in deep marine records due to their condensed nature in combination with chemical and physical mixing processes such as bioturbation. The marine record in Fig. 6 is measured on bulk carbonate instead of a single species, which also contributes to its smooth appearance. The spread in pedogenic $\delta^{13}C$ values found in our record does not reflect seasonal variations, because pedogenic carbonate nodules take decades or more to form (Zamanian et al., 2016) and mixing during this period is expected. Instead, the spread may be explained by nodules of different age occurring at the same level within a paleosol profile, as these may have formed at different depths within a soil. Depth of

soil carbonate formation depends on several factors, such as precipitation, and may have changed over short as well as long time spans in our sections. Soil carbonate usually forms at depths up to 100 to 150 cm, but may form at depths up to 300 cm (Zamanian et al., 2016). This highlights the importance of selecting sites such as the northern Bighorn Basin which are characterized by relatively high accumulation rates, where the length of a precession-related sedimentary cycle significantly exceeds potential fluctuations in carbonate formation depth.

Röhl et al. (2007) constructed cyclostratigraphic age models for deep marine sites and suggested a duration of the CIE body shorter than indicated by the new terrestrial cyclostratigraphic age model (Fig. 6). However, carbonate dissolution by PETM-related ocean acidification reduces the thickness of the CIE interval, leading to potential underestimation of its duration (Röhl et al., 2007). Westerhold et al. (2018) shifted the marine age model by circa 1.5 precession cycle to account for the dissolution and to align the marine age model with their age model for the PCB cores (Fig. 6). Our revised age model shows that the CIE body duration inferred by Westerhold et al. (2018) was slightly overestimated, but confirms their notion that the deep marine record has to be shifted in time.

A recently documented shallow-marine record from the Caucasus in southern Russia shows at least four lithological bands and isotope variations within the CIE body (Shcherbinina et al., 2016). The $\delta^{13}C$ profile indicates that the CIE body continues upward. In this interval, cycles cannot be distinguished with confidence. However, fluctuations in the stable isotope records and carbonate content record suggest that this interval encompasses one additional cycle. This is consistent with our results indicating the body of the CIE encompasses almost exactly 5 precession cycles.

4.4. Pattern and timing of carbon isotope recovery

The $\delta^{13}C$ records of HBSC and PCB show a gradual return to heavier values during most of the CIE body (Fig. 3; Fig. 6). In a way, isotope recovery starts after maximum values are reached shortly after the onset of the PETM. This pattern is interrupted by a short-term positive amplification around 30 kyr after the onset (Fig. 6), of which the origin is unknown. The following steadily increasing but rather stable interval of the main body ends abruptly after 101 kyr with a stepwise shift of 2.7‰ (Fig. 6). Since most other records also show an abrupt rise in $\delta^{13}C$ values at this point, the start of the CIE recovery phase is placed here. The CIE initial recovery step occurs in the Purple-4 paleosol, which according to our results represents an amount of time less than one precession cycle.

Below Purple-4, pedogenic carbonate nodules are abundant and large, whereas in Purple-4 these are nearly absent. Thus, when carbon isotope values increase abruptly, the number and size of nodules decreases. This implies that pedogenic nodule precipitation is related to carbon isotope values in the atmosphere, likely through climate and vegetation feedback effects. However, the presence of nodules depends not only on climate and vegetation, but also on carbonate presence, parent material, and time. Assuming that carbonate presence and parent material did not change over such a short interval, the lack of nodules in Purple-4 provides a strong argument against attributing more time to Purple-4 than to other paleosols in the sections.

Bowen et al. (2015) produced a series of lithology-dependent age models for PCB. Different age model versions vary because absolute deposition rates are unknown. Assuming a one-third over two-third time division between the avulsion and overbank phases, there is approximately 14 kyr in the series of paleosols that constitute the overbank phase. On average, there are three paleosols in one overbank phase, with usually one being distinctly better-developed (Fig. 3; Abels et al., 2013). Considering the previous calculation, the best-developed paleosol in an overbank phase represents between 5 and 10 kyr, possibly up to 15 kyr.

A return of $\delta^{13}C$ to heavier values within 5 to 15 kyr in a single paleosol profile implies even more rapid carbon sequestration than previously suggested (Bowen and Zachos, 2010). A step at the start of the recovery has not been recognized before in a Bighorn Basin isotope record (Koch et al., 1992, 1995; Bowen et al., 2001; Bains et al., 2003; Magioncalda et al., 2004; Bowen et al., 2015), because of the lower resolution of those records. The series we produced in the course of this study seemed to follow the exponential decay curve proposed by Bowen and Zachos (2010) based on an earlier $\delta^{13}C$ record (Bowen et al., 2001) and age model (Abdul Aziz et al., 2008). However, when many more nodules were analyzed, two distinct sets of carbon isotope values remained with a gap at Purple-4 (Fig. 3). Observing this step in two sections 8 km apart gives good confidence that this is a real signal, at least in the northern Bighorn Basin.

The cause of the initial recovery step remains elusive. Between the PETM body and recovery, the pedogenic CIE amplification mechanism (Bowen et al., 2004; Smith et al., 2007; Abels et al., 2016) may have disappeared, explaining part of the magnitude of the step. Still, conditions changed unexpectedly rapid at the time of the IRS, as indicated by the near-disappearance of carbonate nodules. At the same time, Purple-4 marks the end of the PETM body showing intense pedogenesis. Local climate reconstructions and high-resolution isotope records at other continental locations are required to verify the significance of the IRS found in northern Wyoming, and to corroborate the suggested rapid climate change.

4.5. Pattern and timing of mammal recovery

The Paleocene–Eocene Thermal Maximum had a severe impact on the mammalian community. Besides the origination of new mammal taxa, the fauna shows strong dwarfing that is related to warming during the PETM (Gingerich, 1989, 2003; Secord et al., 2012). Faunal zone Wa-1 shows no dwarfed animals, and the Wa-0 to Wa-1 transition may be regarded as the interval of mammalian recovery from dwarfing. Our results show that the faunal recovery from dwarfed species starts circa one precession cycle before the IRS at the end of the PETM body, and faunal recovery is completed during the IRS with Wa-1 fauna directly overlying the IRS. This finding considerably refines earlier observations (Bowen et al., 2001; Wood et al., 2008). Faunal evolution from Wa-0 to Wa-1 involved a transitional fauna that was not recognized before, now classified as a new faunal zone Wa-R (Fig. 7).

From a faunal point of view, the Wa-R zone, which occurs in the end of the PETM body and predates the recovery, is a mirror image of the Wa-M zone (Gingerich and Smith, 2006), which postdates the PETM onset and occurs in the beginning of the body. The transition from a Clarkforkian Cf-3 fauna to a Wasatchian Wa-M fauna roughly coincides with the CIE onset, but the transition from Wa-M to Wa-0 has no obvious correlation with $\delta^{13}C$ change. Similarly, the transition from Wa-0 to Wa-R has no obvious correlation with $\delta^{13}C$ change, but the transition from Wa-R to Wa-1 coincides with the IRS (Fig. 6). Faunal recovery was probably more of a trend than an event, but the paleontological resolution is not yet sufficient to tell the difference.

There are no detailed climate proxy records across the IRS. Clumped isotope reconstructions so far are of very low resolution, and temperature reconstructions are by no means sufficient yet to document a change this rapid (Snell et al., 2013). This means that for now we are left with lithological signs of a PETM body-to-recovery climate transition. The abrupt decrease in number and size of pedogenic nodules as well as the decrease in intensity and thickness of soil profiles after the IRS all point towards a climate transition coeval with $\delta^{13}C$ change. However, we show that initial

readjustments of mammalian fauna, following PETM warming and associated mammalian community changes (Gingerich and Smith, 2006; Secord et al., 2012), started prior to the IRS.

Possibly, as suggested by the faunal transition, climate partly recovered already before the end of the PETM body. Paleosols in the PETM body interval are very thick, well developed, and strongly red and purple in color (Kraus et al., 2013). This character is particularly evident from the base of the Wa-0 zone in the Lower Double-Red paleosols upwards to and including the Upper Double-Red paleosols (Fig. 2; Fig. 3). Paleosol Purple-3 is less thick and distinct, and both Purple-3 and Purple-4 differ chemically from paleosols occurring lower in the PETM body interval (Kraus et al., 2015). Furthermore, paleobotanical records point toward a recovery of precipitation extremes late in the PETM body (Wing et al., 2005), as do ichnofossil assemblages (Smith et al., 2008). Thus, pedogenic, floral, and faunal evidence all suggest that climate returned to more baseline early Eocene conditions during the main body of the PETM before the CIE initial recovery step. The Wa-R transitional fauna may have emerged in line with the recovering climate before the end of the PETM body.

5. Conclusions

Our integrated stratigraphic analyses and carbon isotope profiles of two parallel floodplain records across the Paleocene–Eocene Thermal Maximum in the northern Bighorn Basin, Wyoming, shed new light on the study of such records, on the age model for the PETM, on the shape of the PETM carbon isotope excursion and particularly its recovery, and on the recovery of mammals from greenhouse warming during the PETM. We demonstrate that cyclostratigraphic analyses of fluvial sediments require multiple, parallel sites. Furthermore, these analyses should take into account the sedimentary facies to determine cycle transitions, since fluvial depositional environments are sensitive to internal processes, particularly on shorter time scales. The use of bandpass filters alone is insufficient to produce reliable astronomical age models in fluvial strata. Geochemical records, such as carbon isotope series, should also be produced at high resolution and in parallel sites, because fluvial sedimentation occurs in pulses, with periods of non-deposition and erosion.

We developed a floating astronomical age model, based on sedimentological interpretation of facies alternations and correlation between the sections, and used this model to plot our isotope measurements against time. This yields a composite record of the CIE at unprecedented temporal resolution, showing a CIE body of 101 ± 9 kyr and a recovery interval of 40 or 120 kyr, depending on placement of the end of the recovery. These estimates are in line with and refine previous estimates for the event. The end of the CIE body is characterized by an initial recovery step (IRS) of $+2.7 \pm 1.0‰$. There is no evidence for a large hiatus at this stratigraphic level and we estimate the step to occur within 5 to 15 kyr.

Mammalian recovery from Wa-0 to Wa-1 faunal zones, reported as a new transitional zone that we call Wa-R, starts within the PETM body. Local paleoenvironmental changes point to a climate transition coeval with the IRS, implying that mammalian communities were able to readjust before climate recovered from greenhouse warming. Alternatively, the occurrence of Wa-R fauna indicates that climate partly recovered from PETM extremes already during the main body of the event before the IRS. The latter is in line with earlier studies focusing on soil characteristics, flora, and ichnofauna in the PETM interval in the Bighorn Basin.

Declaration of competing interest

The authors declare that they have no known competing financial interests or personal relationships that could have appeared to influence the work reported in this paper.

Acknowledgements

For field assistance, we sincerely acknowledge the Churchill family of Powell, Wyoming, as well as Niels de Winter, Matthew Gingerich, Jelmer Laks, Lars Noorbergen, Sander Smeets, and Peter van den Berg. For laboratory assistance, we acknowledge Anne Dorst, Mariana Florez, Minke Jansen, Grace Kim, Ben Mengers, Emma Mouthaan, and Arnold van Dijk. We thank Scott Wing for discussions on the PETM in the Bighorn Basin sedimentary record. This research was partially funded by an NWO-ALW VENI grant to HAA (project number 863.11.006) and an NWO-ALW VICI grant to LJL (project number 865.10.001). Field research on the Paleocene–Eocene faunal transition has been supported by a series of grants from the U.S. National Science Foundation, most recently EAR-0125502 and EAR-0958821. Fossils are collected under U.S. Bureau of Land Management Paleontological Resources permit 100-WY-PA94 to PDG.

Appendix A. Supplementary material

Supplementary material related to this article can be found online at https://doi.org/10.1016/j.epsl.2019.116044.

References

Abdul Aziz, H., Hilgen, F.J., van Luijk, G.M., Sluijs, A., Kraus, M.J., Pares, J.M., Gingerich, P.D., 2008. Astronomical climate control on paleosol stacking patterns in the upper Paleocene–lower Eocene Willwood Formation, Bighorn Basin, Wyoming. Geology 36, 531–534. https://doi.org/10.1130/G24734A.1.

Abels, H.A., Clyde, W.C., Gingerich, P.D., Hilgen, F.J., Fricke, H.C., Bowen, G.J., Lourens, L.J., 2012. Terrestrial carbon isotope excursions and biotic change during Palaeogene hyperthermals. Nat. Geosci. 5, 326–329. https://doi.org/10.1038/ngeo1427.

Abels, H.A., Kraus, M.J., Gingerich, P.D., 2013. Precession-scale cyclicity in the fluvial lower Eocene Willwood Formation of the Bighorn Basin, Wyoming (USA). Sedimentology 60, 1467–1483. https://doi.org/10.1111/sed.12039.

Abels, H.A., Lauretano, V., van Yperen, A.E., Hopman, T., Zachos, J.C., Lourens, L.J., Gingerich, P.D., Bowen, G.J., 2016. Environmental impact and magnitude of paleosol carbonate carbon isotope excursions marking five early Eocene hyperthermals in the Bighorn Basin, Wyoming. Clim. Past 12, 1151–1163. https://doi.org/10.5194/cp-12-1151-2016.

Bains, S., Corfield, R.M., Norris, R.D., 1999. Mechanisms of climate warming at the end of the Paleocene. Science 285, 724–727. https://doi.org/10.1126/science.285.5428.724.

Bains, S., Norris, R.D., Corfield, R.M., Bowen, G.J., Gingerich, P.D., Koch, P.L., 2003. Marine–terrestrial linkages at the Paleocene—Eocene boundary. In: Wing, S.L., Gingerich, P.D., Schmitz, B., Thomas, E. (Eds.), Causes and Consequences of Globally Warm Climates in the Early Paleogene. In: Geological Society of America Special Paper, vol. 369, pp. 1–10.

Bowen, G.J., Koch, P.L., Gingerich, P.D., Norris, R.D., Bains, S., Corfield, R.M., 2001. Refined isotope stratigraphy across the continental Paleocene–Eocene boundary on Polecat Bench in the northern Bighorn Basin. In: Gingerich, P.D. (Ed.), Paleocene–Eocene Stratigraphy and Biotic Change in the Bighorn and Clarks Fork Basins, Wyoming. In: University of Michigan Papers on Paleontology, vol. 33, pp. 73–88.

Bowen, G.J., Beerling, D.J., Koch, P.L., Zachos, J.C., Quattlebaum, T., 2004. A humid climate state during the Palaeocene/Eocene thermal maximum. Nature 432, 495–499. https://doi.org/10.1038/nature03115.

Bowen, G.J., Maibauer, B.J., Kraus, M.J., Röhl, U., Westerhold, T., Steimke, A., Gingerich, P.D., Wing, S.L., Clyde, W.C., 2015. Two massive, rapid releases of carbon during the onset of the Palaeocene–Eocene Thermal Maximum. Nat. Geosci. 8, 44–47. https://doi.org/10.1038/ngeo2316.

Bowen, G.J., Zachos, J.C., 2010. Rapid carbon sequestration at the termination of the Palaeocene–Eocene Thermal Maximum. Nat. Geosci. 3, 866–869. https://doi.org/10.1038/ngeo1014.

Clyde, W.C., Christensen, K.E., 2003. Testing the relationship between pedofacies and avulsion using Markov analysis. Am. J. Sci. 303, 60–71. https://doi.org/10.2475/ajs.303.1.60.

Clyde, W.C., Gingerich, P.D., 1998. Mammalian community response to the latest Paleocene thermal maximum: an isotaphonomic study in the northern Bighorn Basin, Wyoming. Geology 26, 1011–1014. https://doi.org/10.1130/0091-7613(1998)026<1011:MCRTTL>2.3.CO;2.

Clyde, W.C., Gingerich, P.D., Wing, S.L., Röhl, U., Westerhold, T., Bowen, G., Johnson, K., Baczynski, A.A., Diefendorf, A., McInerney, F., Schnurrenberger, D., Noren, A., Brady, K., Acks, R., Baczynski, A., Belcher, C., Bowen, G., Brady, K., Clyde, W., Collinson, M., D'Ambrosia, A., Denis, E., Freeman, K., Gingerich, P., Harrington, G., Jardine, P., Johnson, K., Kraus, M., Maibauer, B., McInerney, F., Noren, A., Riedel, J., Röhl, U., Schnurrenberger, D., Schouten, S., Tsukui, K., Weijers, J., Welter, G., Westerhold, T., Wing, S., Wittkopp, F., Wood, A., 2013. Bighorn Basin Coring Project (BBCP): a continental perspective on early Paleogene hyperthermals. Sci. Drill. 16, 21–31. https://doi.org/10.5194/sd-16-21-2013.

Foreman, B.Z., 2014. Climate-driven generation of a fluvial sheet sand body at the Paleocene–Eocene boundary in northwest Wyoming (USA). Basin Res. 26, 225–241. https://doi.org/10.1111/bre.12027.

Foreman, B.Z., Straub, K.M., 2017. Autogenic geomorphic processes determine the resolution and fidelity of terrestrial paleoclimate records. Sci. Adv. 3, e1700683. https://doi.org/10.1126/sciadv.1700683.

Gingerich, P.D., 1969. Markov analysis of cyclic alluvial sediments. J. Sediment. Petrol. 39, 330–332. https://doi.org/10.1306/74D71C4E-2B21-11D7-8648000102C1865D.

Gingerich, P.D., 1989. New Earliest Wasatchian Mammalian Fauna from the Eocene of Northwestern Wyoming: Composition and Diversity in a Rarely Sampled High-Floodplain Assemblage. University of Michigan Papers on Paleontology, vol. 28, pp. 1–97.

Gingerich, P.D., 2001. Biostratigraphy of the continental Paleocene–Eocene boundary interval on Polecat Bench in the northern Bighorn Basin. In: Gingerich, P.D. (Ed.), Paleocene–Eocene Stratigraphy and Biotic Change in the Bighorn and Clarks Fork Basins, Wyoming. In: University of Michigan Papers on Paleontology, vol. 33, pp. 37–71.

Gingerich, P.D., 2003. Mammalian responses to climate change at the Paleocene–Eocene boundary: Polecat Bench record in the northern Bighorn Basin, Wyoming. In: Wing, S.L., Gingerich, P.D., Schmitz, B., Thomas, E. (Eds.), Causes and Consequences of Globally Warm Climates in the Early Paleogene. In: Geological Society of America Special Paper, vol. 369, pp. 463–478.

Gingerich, P.D., Clyde, W.C., 2001. Overview of mammalian biostratigraphy in the Paleocene–Eocene Fort Union and Willwood formations of the Bighorn and Clarks Fork basins. In: Gingerich, P.D. (Ed.), Paleocene–Eocene Stratigraphy and Biotic Change in the Bighorn and Clarks Fork Basins, Wyoming. In: University of Michigan Papers on Paleontology, vol. 33, pp. 1–14.

Gingerich, P.D., Smith, T., 2006. Paleocene–Eocene land mammals from three new latest Clarkforkian and earliest Wasatchian wash sites at Polecat Bench in the northern Bighorn Basin, Wyoming. In: Contributions from the Museum of Paleontology, vol. 31, pp. 245–303.

Giusberti, L., Rio, D., Agnini, C., Backman, J., Fornaciari, E., Tateo, F., Oddone, M., 2007. Mode and tempo of the Paleocene–Eocene thermal maximum in an expanded section from the Venetian pre-Alps. Bull. Geol. Soc. Am. 119, 391–412. https://doi.org/10.1130/B25994.1.

Kennett, J.P., Stott, L.D., 1991. Abrupt deep-sea warming, palaeoceanographic changes and benthic extinctions at the end of the Palaeocene. Nature 353, 225–229. https://doi.org/10.1038/353225a0.

Koch, P.L., Zachos, J.C., Dettman, D.L., 1995. Stable isotope stratigraphy and paleoclimatology of the Paleogene Bighorn Basin (Wyoming, USA). Palaeogeogr. Palaeoclimatol. Palaeoecol. 115, 61–89. https://doi.org/10.1016/0031-0182(94)00107-J.

Koch, P.L., Zachos, J.C., Gingerich, P.D., 1992. Correlation between isotope records in marine and continental carbon reservoirs near the Paleocene–Eocene boundary. Nature 358, 319–322. https://doi.org/10.1038/358319a0.

Kraus, M.J., Aslan, A., 1993. Eocene hydromorphic paleosols: significance for interpreting ancient floodplain processes. J. Sediment. Petrol. 63, 453–463. https://doi.org/10.1306/D4267B22-2B26-11D7-8648000102C1865D.

Kraus, M.J., McInerney, F.A., Wing, S.L., Secord, R., Baczynski, A.A., Bloch, J.I., 2013. Paleohydrologic response to continental warming during the Paleocene–Eocene Thermal Maximum, Bighorn Basin, Wyoming. Palaeogeogr. Palaeoclimatol. Palaeoecol. 370, 196–208. https://doi.org/10.1016/j.palaeo.2012.12.008.

Kraus, M.J., Woody, D.T., Smith, J.J., Dukic, V., 2015. Alluvial response to the Paleocene–Eocene Thermal Maximum climatic event, Polecat Bench, Wyoming (USA). Palaeogeogr. Palaeoclimatol. Palaeoecol. 435, 177–192. https://doi.org/10.1016/j.palaeo.2015.06.021.

Li, M., Hinnov, L., Kump, L., 2019. Acycle: time-series analysis software for paleoclimate research and education. Comput. Geosci. 127, 12–22. https://doi.org/10.1016/j.cageo.2019.02.011.

Magioncalda, R., Dupuis, C., Smith, T., Steurbaut, E., Gingerich, P.D., 2004. Paleocene–Eocene carbon isotope excursion in organic carbon and pedogenic carbonate: direct comparison in a continental stratigraphic section. Geology 32, 553–556. https://doi.org/10.1130/G20476.1.

McInerney, F.A., Wing, S.L., 2011. The Paleocene–Eocene Thermal Maximum: a perturbation of carbon cycle, climate, and biosphere with implications for the future. Annu. Rev. Earth Planet. Sci. 39, 489–516. https://doi.org/10.1146/annurev-earth-040610-133431.

Murphy, B.H., Farley, K.A., Zachos, J.C., 2010. An extraterrestrial ^{3} He-based timescale for the Paleocene–Eocene Thermal Maximum (PETM) from Walvis Ridge, IODP Site 1266. Geochim. Cosmochim. Acta 74, 5098–5108. https://doi.org/10.1016/j.gca.2010.03.039.

Neasham, J.W., Vondra, C.F., 1972. Stratigraphy and petrology of the lower Eocene Willwood Formation, Bighorn Basin, Wyoming. Geol. Soc. Am. Bull. 83, 2167–2180. https://doi.org/10.1130/0016-7606(1972)83[2167:SAPOTL]2.0.CO;2.

Paillard, D.L., Labeyrie, L., Yiou, P., 1996. Macintosh program performs time-series analysis. Eos, Trans. Am. Geophys. Union 77, 379. https://doi.org/10.1029/96EO00259.

Röhl, U., Westerhold, T., Bralower, J.C., Zachos, J.C., 2007. On the duration of the Paleocene–Eocene Thermal Maximum (PETM). Geochem. Geophys. Geosyst. 8, 1–13. https://doi.org/10.1029/2007GC001784.

Secord, R., Bloch, J.I., Chester, S.G.B., Boyer, D.M., Wood, A.R., Wing, S.L., Kraus, M.J., McInerney, F.A., Krigbaum, J., 2012. Evolution of the earliest horses driven by climate change in the Paleocene–Eocene Thermal Maximum. Science 335, 959–962. https://doi.org/10.1126/science.1213859.

Shcherbinina, E., Gavrilov, Y., Iakovleva, A., Pokrovsky, B., Golovanova, O., Aleksandrova, G., 2016. Environmental dynamics during the Paleocene–Eocene thermal maximum (PETM) in the northeastern Peri-Tethys revealed by high-resolution micropalaeontological and geochemical studies of a Caucasian key section. Palaeogeogr. Palaeoclimatol. Palaeoecol. 456, 60–81. https://doi.org/10.1016/j.palaeo.2016.05.006.

Sluijs, A., Bowen, G.J., Brinkhuis, H., Lourens, L.J., Thomas, E., 2007. The Palaeocene–Eocene Thermal Maximum super greenhouse: biotic and geochemical signatures, age models and mechanisms of global change. In: Williams, M., Haywood, A.M., Gregory, F.J., Schmidt, D.N. (Eds.), Deep Time Perspectives on Climate Change: Marrying the Signal From Computer Models and Biological Proxies. The Micropalaeontological Society, Special Publications, The Geological Society, London, pp. 323–347.

Smith, F.A., Wing, S.L., Freeman, K.H., 2007. Magnitude of the carbon isotope excursion at the Paleocene–Eocene thermal maximum: the role of plant community change. Earth Planet. Sci. Lett. 262, 50–65. https://doi.org/10.1016/j.epsl.2007.07.021.

Smith, J.J., Hasiotis, S.T., Kraus, M.J., Woody, D.T., 2008. Relationship of floodplain ichnocoenoses to paleopedology, paleohydrology, and paleoclimate in the Willwood Formation, Wyoming, during the Paleocene–Eocene Thermal Maximum. Palaios 23, 683–699. https://doi.org/10.2110/palo.2007.p07-080r.

Snell, K.E., Thrasher, B.L., Eiler, J.M., Koch, P.L., Sloan, L.C., Tabor, N.J., 2013. Hot summers in the Bighorn Basin during the early Paleogene. Geology 41, 55–58. https://doi.org/10.1130/G33567.1.

Torrence, C., Compo, G.P., 1998. A practical guide to wavelet analysis. Bull. Am. Meteorol. Soc. 79, 61–78. https://doi.org/10.1175/1520-0477(1998)079<0061:APGTWA>2.0.CO;2.

Westerhold, T., Röhl, U., Wilkens, R.H., Gingerich, P.D., Clyde, W.C., Wing, S.L., Bowen, G.J., Kraus, M.J., 2018. Synchronizing early Eocene deep-sea and continental records – cyclostratigraphic age models for the Bighorn Basin Coring Project drill cores. Clim. Past 14, 303–319. https://doi.org/10.5194/cp-14-303-2018.

Wing, S.L., Harrington, G.J., Smith, F.A., Bloch, J.I., Boyer, D.M., Freeman, K.H., 2005. Transient floral change and rapid global warming at the Paleocene–Eocene boundary. Science 310, 993–996. https://doi.org/10.1126/science.1116913.

Wood, A.R., Kraus, M.J., Gingerich, P.D., 2008. Downslope fossil contamination: mammal-bearing fluvial conglomerates and the Paleocene–Eocene faunal transition (Willwood Formation, Bighorn Basin, Wyoming). Palaios 23, 380–390. https://doi.org/10.2110%2Fpalo.2007.p07-045r.

Zachos, J.C., Dickens, G.R., Zeebe, R.E., 2008. An early Cenozoic perspective on greenhouse warming and carbon-cycle dynamics. Nature 451, 279–283. https://doi.org/10.1038/nature06588.

Zamanian, K., Pustovoytov, K., Kuzyakov, Y., 2016. Pedogenic carbonates: forms and formation processes. Earth-Sci. Rev. 157, 1–17. https://doi.org/10.1016/j.earscirev.2016.03.003.

Zeebe, R., Zachos, J.C., Dickens, G.R., 2009. Carbon dioxide forcing alone insufficient to explain Palaeocene–Eocene Thermal Maximum warming. Nat. Geosci. 2, 576–580. https://doi.org/10.1038/ngeo578.